



Kinematic Decomposition of IllustrisTNG Disk Galaxies: Morphology and Relation with Morphological Structures

Min Du¹ , Luis C. Ho^{1,2} , Victor P. Debattista³ , Annalisa Pillepich⁴ , Dylan Nelson⁵, Dongyao Zhao¹ , and Lars Hernquist⁶ 

¹ Kavli Institute for Astronomy and Astrophysics, Peking University, Beijing 100871, People's Republic of China; dumin@pku.edu.cn

² Department of Astronomy, School of Physics, Peking University, Beijing 100871, People's Republic of China

³ Jeremiah Horrocks Institute, University of Central Lancashire, Preston PR1 2HE, UK

⁴ Max-Planck-Institut für Astronomie, Königstuhl 17, D-69117 Heidelberg, Germany

⁵ Max-Planck-Institut für Astrophysik, Karl-Schwarzschild-Str. 1, D-85741 Garching, Germany

⁶ Harvard-Smithsonian Center for Astrophysics, 60 Garden Street, Cambridge, MA 02138, USA

Received 2020 February 8; revised 2020 May 1; accepted 2020 May 1; published 2020 June 4

Abstract

We recently developed an automated method, `auto-GMM`, to decompose simulated galaxies. It extracts kinematic structures in an accurate, efficient, and unsupervised way. We use `auto-GMM` to study the stellar kinematic structures of disk galaxies from the TNG100 run of *IllustrisTNG*. We identify four to five structures that are commonly present among the diverse galaxy population. Structures having strong to moderate rotation are defined as cold and warm disks, respectively. Spheroidal structures dominated by random motions are classified as bulges or stellar halos, depending on how tightly bound they are. Disky bulges are structures that have moderate rotation but compact morphology. Across all disk galaxies and accounting for the stellar mass within 3 half-mass radii, the kinematic spheroidal structures, obtained by summing up stars of bulges and halos, contribute $\sim 45\%$ of the total stellar mass, while the disk structures constitute $\sim 55\%$. This study also provides important insights into the relationship between kinematically and morphologically derived galactic structures. Comparing the morphology of kinematic structures with that of traditional bulge+disk decomposition, we conclude that (1) the morphologically decomposed bulges are composite structures comprising a slowly rotating bulge, an inner halo, and a disk bulge; (2) kinematically disk bulges, akin to what are commonly called pseudo-bulges in observations, are compact disk-like components that have rotation similar to warm disks; (3) halos contribute almost 30% of the surface density of the outer part of morphological disks when viewed face on; and (4) both cold and warm disks are often truncated in central regions.

Unified Astronomy Thesaurus concepts: [Disk galaxies \(391\)](#); [Galaxy structure \(622\)](#); [Hydrodynamical simulations \(767\)](#); [Galaxy dynamics \(591\)](#); [Galaxy kinematics \(602\)](#)

1. Introduction

Classification of galaxies is one of the most fundamental and important steps in understanding galaxy evolution. The decomposition of galaxies into a bulge and a disk component serves as a foundation for the classification of galaxies into the Hubble (1926) sequence (Sandage et al. 1981), even if galaxies often comprise additional structures. For example, the Milky Way is a prototypical spiral galaxy exhibiting several stellar components, including a thin and thick disk, a boxy/peanut-shaped bulge, a bar, a stellar halo, and a nuclear star cluster (see the review by Bland-Hawthorn & Gerhard 2016). Many nearby galaxies that can be well-resolved in detail also have a thick disk that is old and metal poor with respect to the thin disk (Dalcanton & Bernstein 2002; Yoachim & Dalcanton 2006; Comerón et al. 2011, 2014; Elmegreen et al. 2017). Meanwhile, the morphology of bulges covers a broad range, from highly spherically symmetric to flat (Andredakis & Sanders 1994; Andredakis et al. 1995; Courteau et al. 1996; Méndez-Abreu et al. 2010). Classical bulges, likely the end-products of galaxy mergers (Toomre 1977), are expected to be dynamically hot, spheroidal, and centrally concentrated. More flattened, rotationally supported spheroids, named pseudo-bulges, are expected to be an outcome of internal secular processes (e.g., Kormendy & Kennicutt 2004). The rich diversity of structures observed among nearby galaxies is evidence of the complex formation and evolutionary history of galaxies. To understand the formation and evolution of galaxies,

accurate recognition and decomposition of structures are essential; this, however, is a very challenging task due to the incomplete information that can be inferred from observations and, in particular, to the confusion from line-of-sight projection.

Galaxies can be better characterized and decomposed when information about their internal kinematics is observationally available. The rapid development of integral-field unit (IFU) spectroscopy (e.g., Emsellem et al. 2007, 2011; Cappellari et al. 2011a, 2011b) has led to rapid progress in decomposing galaxies with the aid of kinematical information. Zhu et al. (2018c) first applied the orbit-superposition method (e.g., Schwarzschild 1979; Valluri et al. 2004; van den Bosch et al. 2008) to reconstruct stellar orbits based on the stellar kinematics of galaxies in the CALIFA survey (Sánchez et al. 2012) and was therefore able to successfully extract kinematically cold, warm, hot, and counterrotating components (Zhu et al. 2018a, 2018b). Recently, Zhu et al. (2019) further included the stellar population distribution in modeling galaxies.

The development of kinematic decomposition helps to break the degeneracy in morphology of different structures identified by the distribution of stellar mass or light. For instance, contrary to expectations from morphological decomposition (e.g., Fisher & Drory 2008, but see Gao et al. 2020), recent kinematic studies found no clear correlation between the Sérsic index n and galactic kinematic properties derived with the IFU

technique (e.g., Krajnović et al. 2013; Schulze et al. 2018). Zhu et al. (2018a) also suggested that n is not a good discriminator between rotating pseudo-bulges and classical bulges with weak rotation. Therefore, it is crucial to elucidate the intrinsic relationship between kinematic structures and the more familiar, traditional morphological structures.

Notwithstanding the advances enabled by IFU spectroscopy, the level of detail in which galaxies can be decomposed based on observations remains quite restrictive. Complementary progress can be made by turning to large-scale hydrodynamical cosmological simulations, which self-consistently capture the properties of the stellar and gaseous components of galaxies. As well-informed spectators, we can extract intrinsic structures in simulated galaxies and track their evolutionary history. In recent years, significant progress has been made in modeling star formation and stellar feedback in simulations (Agertz et al. 2011; Guedes et al. 2011; Aumer et al. 2013; Stinson et al. 2013; Marinacci et al. 2014; Roškar et al. 2014; Murante et al. 2015; Colín et al. 2016; Grand et al. 2017), to the point that galaxies with realistic bulge+disk structures can be reproduced in a fully cosmological context, including Illustris (Genel et al. 2014; Vogelsberger et al. 2014a, 2014b; Nelson et al. 2015) and its follow-up project IllustrisTNG (Marinacci et al. 2018; Naiman et al. 2018; Nelson et al. 2018, 2019c; Pillepich et al. 2018a, 2019; Springel et al. 2018), EAGLE (Crain et al. 2015; Schaye et al. 2015), and Horizon-AGN (Dubois et al. 2016); see the review by Vogelsberger et al. (2020). Galaxy zoom-in simulations, such as Auriga (Grand et al. 2017), FIRE (Hopkins et al. 2014, 2018), and NIHAO (Wang et al. 2015), have been able to generate galaxies with multiple structures beyond the simple bulge+disk components (e.g., Brook et al. 2012; Algorry et al. 2017; Ma et al. 2017; Obreja et al. 2019; Gargiulo et al. 2019). Recently, the highest resolution run of the IllustrisTNG (TNG50) simulated a fully representative cosmological volume of $(50 \text{ Mpc})^3$ at a resolution comparable to that of zoom-in simulations (Nelson et al. 2019a; Pillepich et al. 2019). In light of this development, a modern method that can decompose intrinsic structures in a physical way beyond the most basic bulge+disk components is required to make full use of the power of hydrodynamical cosmological simulations.

Du et al. (2019) presented a fully automated method, `auto-GMM`, to identify different kinematic components of a galaxy accurately and efficiently. Gaussian mixture models in `auto-GMM` serve as an unsupervised machine-learning algorithm to isolate distinct structures in the kinematic phase space of simulated galaxies (see also Obreja et al. 2016, 2018). We automated the code to determine the number of Gaussian components allowed by the data through a modified Bayesian information criterion (BIC). As a result, the possibility of human bias is minimized using this method. As shown in Du et al. (2019), `auto-GMM` successfully identifies kinematic structures in galaxies with diverse morphological and kinematic properties.

Thanks to an updated galaxy physics model (Weinberger et al. 2017; Pillepich et al. 2018b), galaxies in IllustrisTNG successfully capture many of the observed optical morphologies of nearby galaxies (Huertas-Company et al. 2019; Rodriguez-Gomez et al. 2019). The realism of the mock galaxies inspires confidence that the latest simulations can be used for detailed statistical studies and to inform the correlation between kinematically and morphologically defined galaxy components. In this work, we apply `auto-GMM` to a large

sample of galaxies from the TNG100 run of the IllustrisTNG simulations.

This paper is organized as follows. Our methodology is demonstrated in Section 2. Section 3 introduces the sample of disk galaxies used in our analysis. The two methods used to classify structures found in kinematic phase space are described in Section 4. The basic morphological properties of such kinematic structures⁷ are shown in Section 5 and compared with the bulge+disk structures decomposed based on morphology. Our conclusions are summarized in Section 6.

2. Methodology of Kinematic Decomposition

It is natural that stars belonging to the same physical structure should cluster in their kinematic phase space. We characterize each star by three dimensionless parameters in kinematic phase space: the circularity parameter $\epsilon = j_z/j_c(e)$ (Abadi et al. 2003), nonazimuthal angular momentum $j_p/j_c(e)$, and binding energy normalized by the minimum value $e/|e|_{\max}$, as proposed by Doménech-Moral et al. (2012). The specific azimuthal angular momentum j_z and nonazimuthal angular momentum j_p are normalized by j_c , the maximum angular momentum having the same specific binding energy e . The maximum value of $|e|$ across the whole galaxy, $|e|_{\max}$, corresponds to the energy of the star that is most tightly bound at the galactic center. Thus, j_z/j_c and j_p/j_c quantify the aligned and misaligned rotation with the overall angular momentum, respectively, and $e/|e|_{\max}$ describes how tightly bound a stellar particle is. Consequently, the same standard is used to describe the kinematic properties of stars in diverse galaxies across the full mass range. All galaxies are oriented with their total angular momentum along the z -axis. We apply the code from Obreja et al. (2018) to build the kinematic phase space of j_z/j_c , j_p/j_c , and $e/|e|_{\max}$ for all stars gravitationally bound to the galaxy with no limitation in galactocentric distance in individual galaxies, assuming every galaxy is isolated.

We employ `auto-GMM` to identify structures through the clustering of the kinematic phase-space parameters for all stars in each galaxy. `auto-GMM` is developed by combining the `GaussianMixture` module from the PYTHON `scikit-learn` package (Pedregosa et al. 2011) with a modified BIC (Du et al. 2019, see Section 2.3). We briefly summarize this method here. The procedure is the same as that in Du et al. (2019). The `GaussianMixture` module is an unsupervised machine-learning algorithm that clusters data efficiently to a target number of Gaussian components. Unlike most nonparametric clustering techniques that give “hard” assignments of stars to components, the parametric GMM approach allows “soft” probabilistic assignments. Each Gaussian component is a triaxial ellipsoid in the three-dimensional kinematic phase space. As recommended by Du et al. (2019), we allow the number of Gaussian components to be determined automatically by the modified ΔBIC , with the criterion $\Delta\text{BIC} < C_{\text{BIC}}$. We defined ΔBIC as $\text{BIC} - \text{BIC}_{\min}$, where BIC_{\min} corresponds to the “ideal” model having numerous Gaussian components. For the large data sample of stars in any galaxy, ΔBIC is approximately equal to $-2\ln \text{BF}$. Here, BF is the Bayes factor (Kass & Raftery 1995) that can be used to quantify the evidence for the multiple Gaussian models `auto-GMM` found, compared to the perfect model. For two identical models, BF is

⁷ The mass fraction and images of each kinematic structure are publicly available at www.tng-project.org/data/.

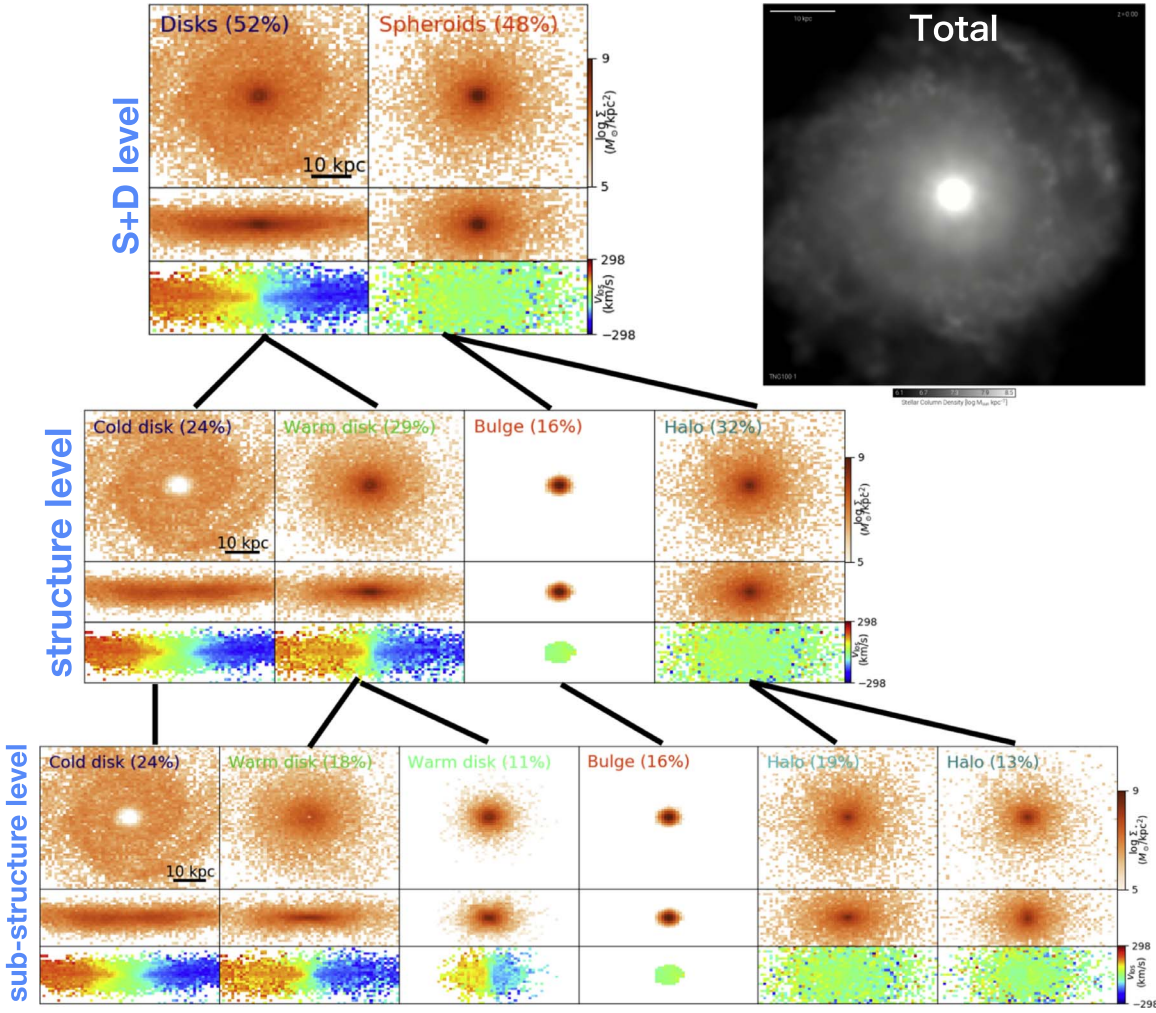


Figure 1. Illustration of the hierarchical framework to understand galaxies with `auto-GMM` for a typical disk galaxy (ID 96505) in TNG100. The top-right panel shows the face-on smoothed stellar column density of all stars produced by the `IllustrisTNG` online visualization tool. The other three rows correspond to three levels of detail decomposed by `auto-GMM`: the spheroid+disk (S+D) level, the structure level, and the substructure level. Each row shows, from top to bottom, the face-on and edge-on views of the surface density distribution, and the edge-on mean velocity distribution. The structures at each lower level merge into the same structure in the higher level based on their similarities in kinematics. The structure classification used here uses classification method 1 described in Section 4.1. We regard the S+D level of the kinematic decomposition as the counterpart of the morphological bulge+disk decomposition. In this paper, we will not make use of the substructure-level detail. Images of all disk galaxies are released on the `IllustrisTNG` website, <https://www.tng-project.org/data/docs/specifications/>.

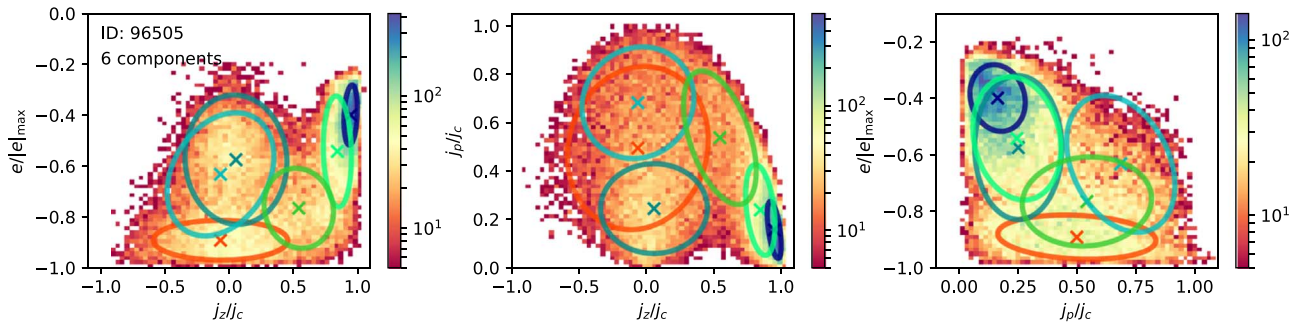


Figure 2. Kinematic phase space (j_z/j_c , j_p/j_c , and $e/|e|_{\max}$) of the stars in the galaxy shown in Figure 1. The ellipses ($\sim 63\%$ confidence) correspond to the six Gaussian components (the substructure level in Figure 1) in the same color scheme. The crosses mark their centers. The color bars represent the number of stellar particles in each bin.

equal to 1. Here we set $C_{\text{BIC}} = 0.1$, which corresponds to $0.95 < \text{BF} < 1$; this is considered as equally well fitting with respect to the ideal model. As shown in Du et al. (2019), C_{BIC} is the only parameter that introduces a minor artificial effect. A reasonable C_{BIC} can vary in 0.05–0.15, resulting in slightly

more or fewer Gaussian components. This criterion not only successfully avoids overfitting due to the use of too many components, but also minimizes the possibility of human bias. Its automated character enables implementation to a large sample of galaxies from cosmological simulations.

Furthermore, `auto-GMM` serves as a framework for understanding galaxy structures. Realistic galactic structures inevitably contain some degree of finer substructure, not the least of which because the distribution function of structures in galaxies may not follow a simple Gaussian. Multiple Gaussian components, corresponding to substructures, are allowed to exist in the same kinematic structure. Substructures with similar kinematics contribute hierarchically to a higher level of structure. Figure 1 illustrates an example galaxy (ID 96505) from the TNG100 run of `IllustrisTNG` at $z=0$. `auto-GMM` finds six kinematic Gaussian components at the substructure level (bottom panels). The positions of these Gaussian components on the kinematic phase space are shown in Figure 2. The two disk components with a similar circularity parameter are considered as substructures of the same warm disk structure; likewise, the two “halos” at the substructure level belong to the same halo at the structure level. A less prominent Gaussian component induced by using a smaller C_{BIC} will merge with a more certain structure, reducing this artificial effect. The uncertainty in our statistic results due to C_{BIC} is thus negligible. Summing up all disk (cold and warm disks) and spheroidal structures recovers the traditional spheroid+disk decomposition (S+D level).

This work focuses on the morphological properties of the principal structures in the stellar component of simulated galaxies; substructures included in each structure will not be considered further in the following analysis. The criteria used to classify structures will be described in detail in Section 4.

3. Sample Selection of Disk Galaxies

The `IllustrisTNG` Project (Marinacci et al. 2018; Naiman et al. 2018; Nelson et al. 2018, 2019c; Pillepich et al. 2018a, 2019; Springel et al. 2018) is a suite of magnetohydrodynamic cosmological simulations run with the moving-mesh code `AREPO` (Springel 2010; Pakmor et al. 2011, 2016). `IllustrisTNG` has successfully reproduced many fundamental properties and scaling relations of observed galaxies. For example, the mass–size relation observed in both late-type and early-type galaxies has been well recovered within observational uncertainties (Genel et al. 2018; Huertas-Company et al. 2019; Rodriguez-Gomez et al. 2019). In particular, Rodriguez-Gomez et al. (2019) showed that the optical size and shape of the `IllustrisTNG` galaxies are consistent within $\sim 1\sigma$ scatter of the observed trends. Furthermore, Xu et al. (2019) found that the fractions of the different orbital components in `IllustrisTNG` are remarkably consistent with those estimated in `CALIFA` galaxies (Zhu et al. 2018c). Moreover, `Illustris` and `IllustrisTNG` have reproduced galaxies with unusual structural and kinematic properties, such as shell galaxies (Pop et al. 2017, 2018), low surface brightness galaxies (Zhu et al. 2018d), and jellyfish galaxies (Yun et al. 2019). The great success of these simulations gives us confidence that they can be used for statistical studies of kinematic structures and to obtain insights about the relationship between kinematically and morphologically identified structures. To obtain adequate statistics as well as a proper resolution, we analyze the TNG100 run. TNG100 follows the evolution of 2×1820^3 resolution elements within a periodic cube measuring $75 h^{-1} \approx 110.7$ Mpc on a side, which translates to an average baryonic mass resolution

element of $1.39 \times 10^6 M_{\odot}$. The gravitational softening length of the stellar particles is $0.5 h^{-1} \approx 0.74$ kpc.

To ensure that the galaxies have well-resolved structures, we concentrate on subhalos having stellar masses greater than $10^{10} M_{\odot}$, identified by using the friends-of-friends (Davis et al. 1985) and SUBFIND (Springel et al. 2001) algorithms. A total of 6507 galaxies match this criterion. To compare galaxy properties to observations and previous works, most physical properties are measured within three times the three-dimensional half-mass radius, r_e . We verified that the statistic results measured for all stars or for stars within 30 kpc generally show only minor difference from those measured within $3r_e$. We classify selected galaxies into disk and elliptical galaxies according to the relative importance of the kinetic energy in ordered rotation, $K_{\text{rot}} = \langle v_{\phi}^2 / v^2 \rangle$ (Sales et al. 2010), where v_{ϕ} and v are the rotation velocity and total velocity, respectively, for each star. The quantity K_{rot} measures the mass-weighted average value of v_{ϕ}^2 / v^2 within a sphere of 30 kpc for each galaxy. In all, 3931 rotation-dominated galaxies with $K_{\text{rot}} \geq 0.5$ are found; the other ones are classified as ellipticals.

Stars moving on bar orbits generally have significant radial motions, which cause mixing in the kinematic phase space of j_z/j_c and j_p/j_c between disks and spheroids (Du et al. 2019). Thus, the presence of bars likely pollutes any analysis based on kinematic decomposition. Bar structures are commonly present in massive galaxies in TNG100. Rosas-Guevara et al. (2020) found bars in 37% of disk galaxies with total stellar mass $M_{\star} \geq 10^{10.4} M_{\odot}$. In addition, D. Zhao et al. (2020, in preparation), applying the same criterion for selecting disk galaxies as we do, show that the bar fraction reaches 52%, consistent with the results of near-infrared surveys of nearby galaxies (e.g., Eskridge et al. 2000; Knäpen et al. 2000; Marinova & Joojee 2007; Menéndez-Delmestre et al. 2007; Díaz-García et al. 2016; Erwin 2018). A similar conclusion is reached independently by Zhou et al. (2020). Based on the TNG100 galaxy catalog of D. Zhao et al. (2020, in preparation), we further separate disk galaxies into subsamples of barred and unbarred galaxies. Bar structures are identified with the observational criteria used in Marinova & Joojee (2007), based on ellipticity and position angle criteria imposed on isophotal analysis of face-on, mass-based surface density maps: (1) the maximum value of ellipticity is larger than 0.25; meanwhile, the variation of ellipse position angle is less than 10° ; and (2) ellipticity decreases noticeably outward from the maximum. Most galaxies with stellar mass $< 10^{10.5} M_{\odot}$ host bars of half-size radius < 3 kpc. More massive galaxies host longer bars, qualitatively consistent with the observed relation between bar size and galaxy stellar mass (Erwin 2018), though TNG100 overproduces many relatively short bars. We use this subset to investigate the impact of bars on our main results.

4. Intrinsic Structures Found in the Distribution of Kinematic Moments

We construct the distribution of kinematic moments for the Gaussian components obtained from applying `auto-GMM` to all disk galaxies selected from TNG100. The structural kinematic moments are the mass-weighted mean values of the three kinematical phase-space parameters of all stars gravitationally bound to the galaxy in each Gaussian component, $\langle j_z/j_c \rangle$, $\langle j_p/j_c \rangle$, and $\langle e/|e|_{\text{max}} \rangle$.

Intrinsic structures should naturally cluster in structural kinematic moments, in a similar way to what stars do in an

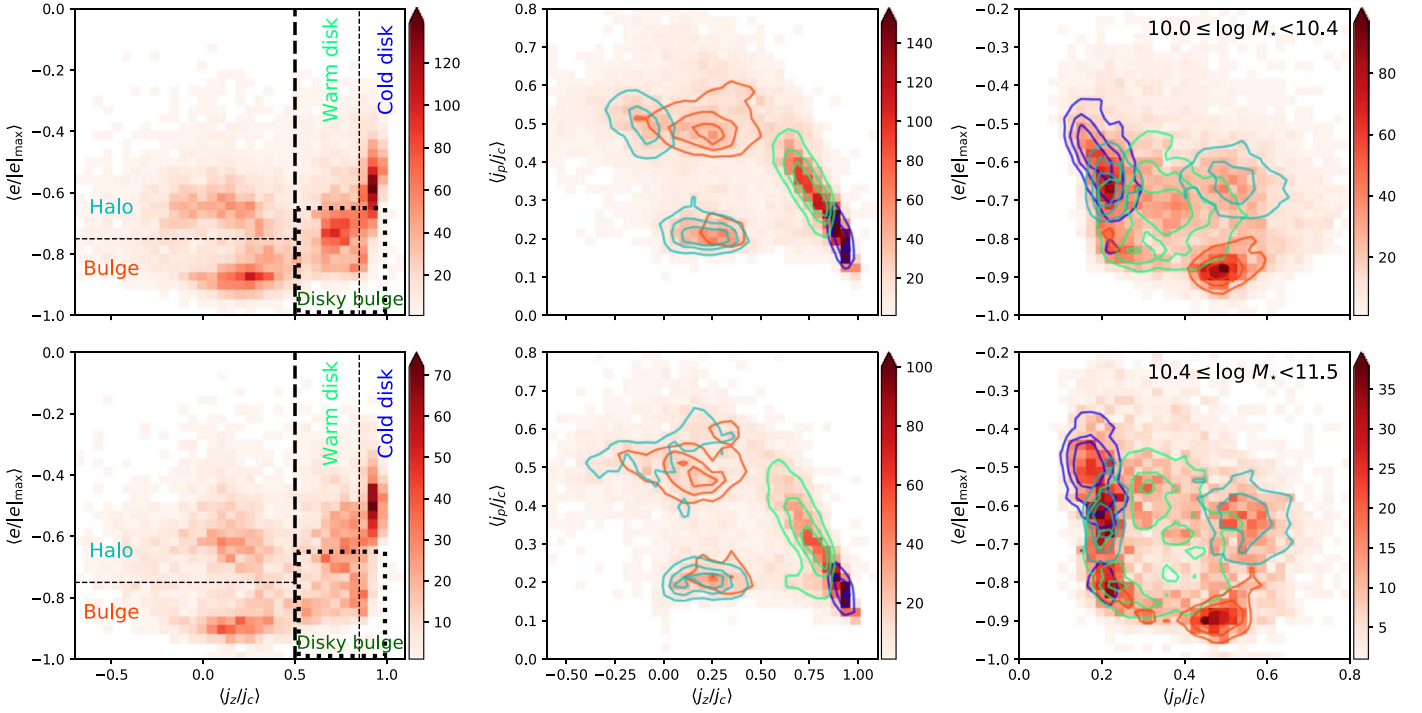


Figure 3. Distribution of structural kinematic moments (average kinematics $\langle j_z/j_c \rangle$, $\langle j_p/j_c \rangle$, and $\langle e/|e|_{\max} \rangle$) of unbarred disk galaxies. Note that the kinematic moments here are the mass-weighted mean values of the three kinematical phase-space parameters of all stars in each Gaussian component. Then, the map represents the distribution of all Gaussian components decomposed by `auto-GMM` for the selected sample of galaxies instead of stars in a single galaxy. The galaxies are separated into mass ranges of (top) $10^{10.0}$ – $10^{10.4} M_\odot$ and (bottom) $10^{10.4}$ – $10^{11.5} M_\odot$. All components found by `auto-GMM` are classified into four kinds of structures in classification 1: cold disk (blue), warm disk (green), bulge (red), or halo (cyan). The contours in the same color show their distributions in maps of (middle) $\langle j_p/j_c \rangle$ versus $\langle j_z/j_c \rangle$ and (right) $\langle j_p/j_c \rangle$ versus $\langle e/|e|_{\max} \rangle$. The classification criteria are marked by the dashed lines. At the S+D level, they are classified into spheroids and disks by $\langle j_z/j_c \rangle = 0.5$. At the structure level, spheroids are classified into halos and bulges using $\langle e/|e|_{\max} \rangle = -0.75$, while disks are classified into cold and warm disks using $\langle j_z/j_c \rangle = 0.85$. The dotted square with $-1.0 \leq \langle e/|e|_{\max} \rangle < -0.65$ and $0.5 \leq \langle j_z/j_c \rangle \leq 1.0$ marks the region of disk galaxies defined in classification 2.

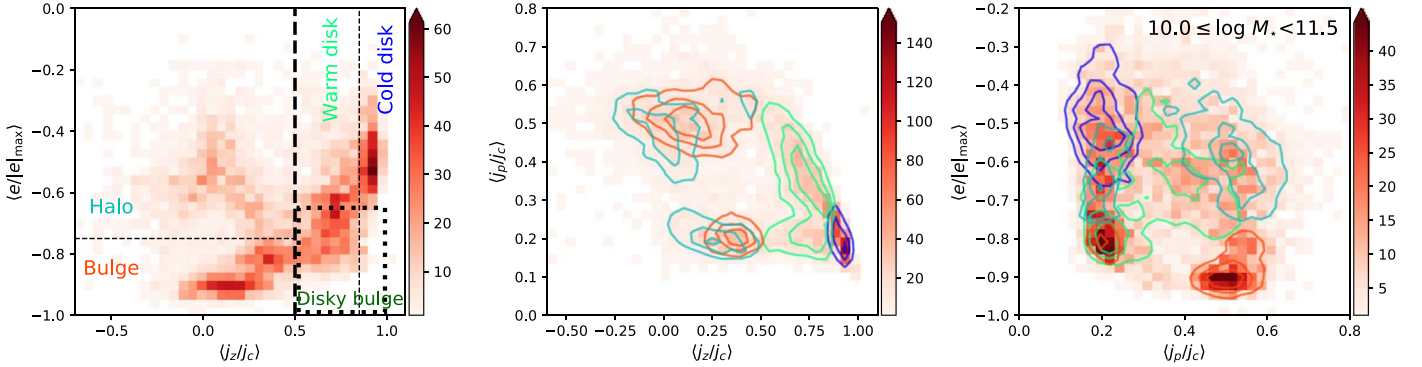


Figure 4. Distribution of kinematic moments (average kinematics $\langle j_z/j_c \rangle$, $\langle j_p/j_c \rangle$, and $\langle e/|e|_{\max} \rangle$) of barred disk galaxies in the mass range $10^{10.0}$ – $10^{11.5} M_\odot$. The classification criteria are the same as those used in Figure 3.

individual galaxy. In this section, we introduce two methods to classify the `auto-GMM` components by their structural kinematic moments.

4.1. Classification 1: Cold/Warm Disk, Bulge, and Halo

Figures 3 and 4 show the structure kinematic phase spaces of unbarred and barred disk galaxies, respectively. Unbarred galaxies are separated into two mass bins, $M_* = 10^{10.0}$ – $10^{10.4} M_\odot$ and $10^{10.4}$ – $10^{11.5} M_\odot$. Four distinguishable clusters, likely corresponding to intrinsic structures, are clearly seen. These features are not significantly affected by the stellar mass of the galaxies or whether they host a bar.

Every `auto-GMM` component can be easily classified into spheroidal or disk structures by setting a circularity criterion $\langle j_z/j_c \rangle = 0.5$ (thick dashed line). We further classify spheroidal components into bulges and halos using the criterion $\langle e/|e|_{\max} \rangle = -0.75$ (horizontal dashed line), while the disk components are classified into cold or warm disks using $\langle j_z/j_c \rangle = 0.85$. These structures also cluster well by introducing the $\langle j_p/j_c \rangle$ dimension (see the contours in the right two panels). In this scheme, which we call classification 1, every galaxy is deconstructed at the structure level or the spheroids+disks (S+D) level (Figure 1). Classification 1 uses the same criteria as those in Du et al. (2019). In previous studies (e.g., Abadi et al. 2003), the bulge is commonly defined as a structure

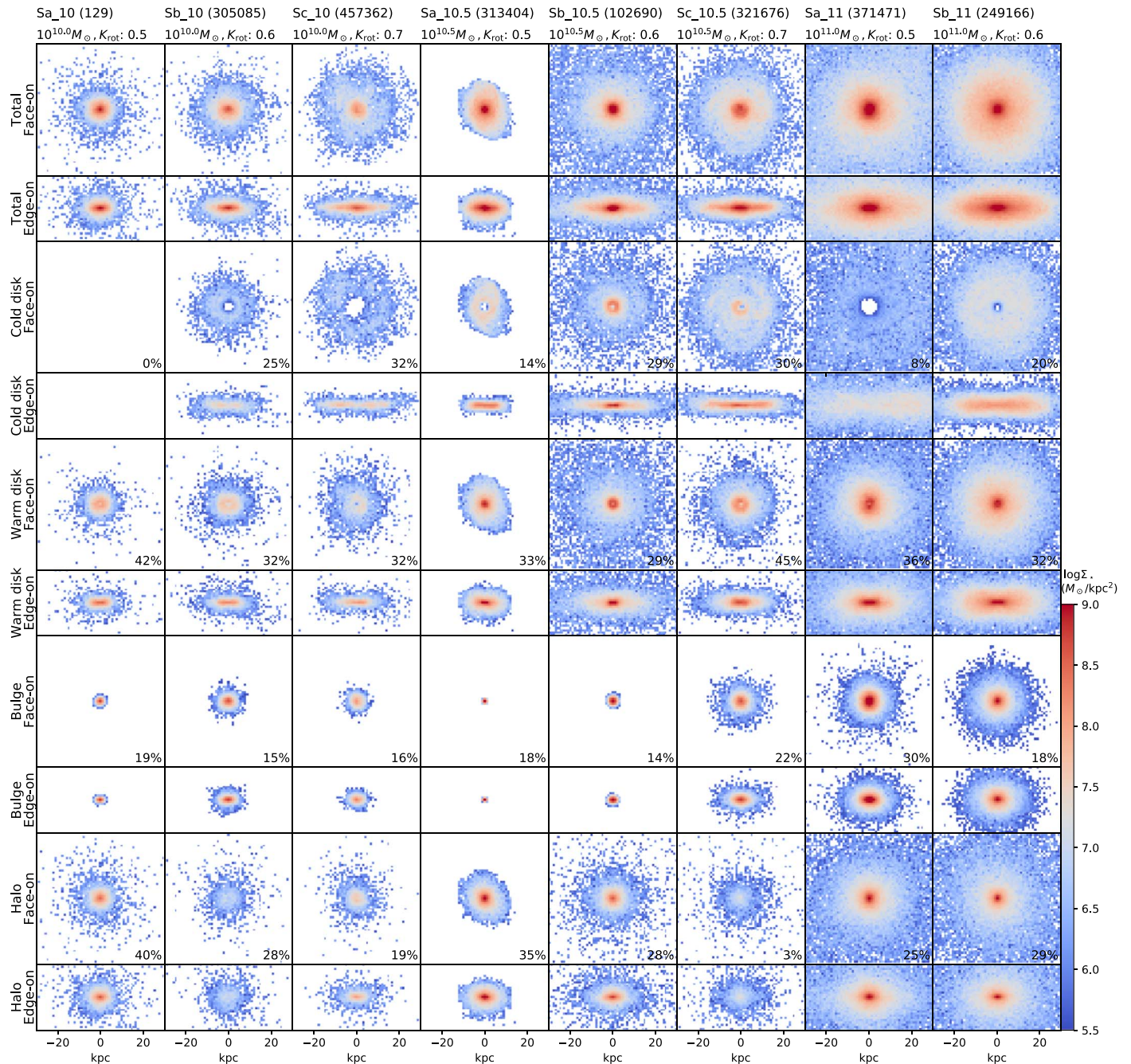


Figure 5. Kinematic structures of example galaxies selected from TNG100 at $z = 0$, classified according to method 1. From top to bottom, we show the face-on and edge-on surface density distributions of the entire galaxy, cold disk, warm disk, bulge, and halo. The bottom-right corner gives the mass fraction of each structure estimated from stars within $3r_c$. We show eight galaxies of different stellar mass ($M_* = 10^{10}$ – $10^{11} M_\odot$) and rotation ($K_{\text{rot}} = 0.5$ – 0.7); see the second row of the header for each column. Few galaxies of $M_* = 10^{11} M_\odot$ have strong rotation, and thus no example is found for $K_{\text{rot}} = 0.7$. The numbers in brackets are the ID of each galaxy in TNG100.

without rotation, in which star particles distribute asymmetrically around $j_z/j_c = 0$. However, the physical justification is debatable. Figure 3 shows that bulge structures cluster around $\langle j_z/j_c \rangle = 0.2$, indicating weak rotation. The assumption of no rotation may significantly underestimate spheroids.

A similar pattern emerges in the structure kinematic phase space of barred galaxies (Figure 4). However, there is no clear boundary that separates warm disks and bulges in barred galaxies, possibly due to the kinematic mixture of stars in the bar. Our adopted kinematic phase space cannot distinguish

ordered radial motions, resulting in the misclassification of some dynamically cold stars into a hotter structure.

Figure 5 shows a few examples of galaxies with $M_* = 10^{10}$, $10^{10.5}$, and $10^{11} M_\odot$ and $K_{\text{rot}} = 0.5$, 0.6 , and 0.7 , randomly selected from the parent sample. From left to right, they can be separated into three groups by mass. Selected galaxies with $K_{\text{rot}} = 0.5$, 0.6 , and 0.7 are named Sa_*, Sb_*, and Sc_*, respectively, where * corresponds to the logarithm of its stellar mass. The visual morphologies of their structures are shown in face-on (upper panels) and edge-on (lower panels)

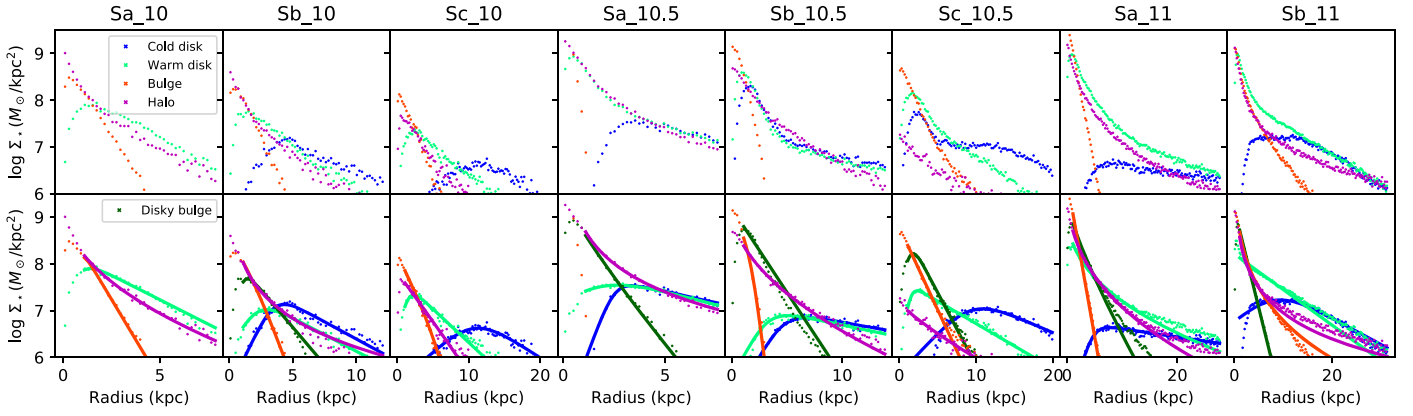


Figure 6. Face-on surface density of the kinematic structures found by `auto-GMM`. The models correspond to the same galaxies shown in Figure 5. The top and bottom panels show the results obtained using classifications 1 and 2, respectively. The points are the surface density viewed face on, averaged within annuli of width 0.2 kpc. The solid profiles in the bottom panels represent the model fit using either a centrally truncated exponential or a Sérsic function. Note that the difference between classifications 1 and 2 arise from whether or not the diskly bulge is considered as a separate structure from the cold and warm disks.

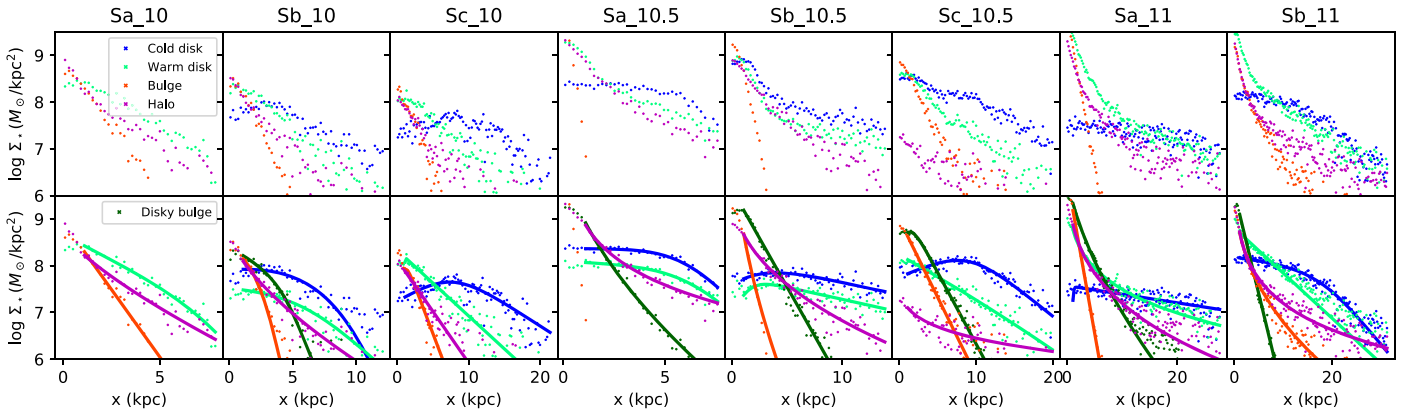


Figure 7. Edge-on surface density profiles of the kinematic structures found by `auto-GMM`. The models correspond to the same galaxies shown in Figures 5 and 6. The top and bottom panels show the results obtained using classifications 1 and 2, respectively. The discrete data are measured from stars within rectangular bins of width $\Delta x = 0.2$ kpc and height $|z| \leq 0.5$ kpc along the major axis in edge-on view. The solid profiles in the bottom panels represent the best-fitting model using either a centrally truncated exponential or a Sérsic function.

views. The top two rows represent the surface density distribution of all stars. It is clear that, with the increase of K_{rot} (from left to right in each group), galaxies having the same mass become more diskly and less compact.

The kinematic structures identified by classification 1 are shown from the third row to the bottom in Figure 5: cold disks, warm disks, bulges, and halos. It is clear that, from a morphological perspective, they are qualitatively consistent with thin disks, thick disks, bulges, and halos. The bottom-right corner of each panel provides the mass ratio of the corresponding structure measured within $3r_e$. The cold disks are the thinnest diskly structure within each galaxy, and commonly host spiral arms (e.g., Sa_10.5 and Sc_10.5). The warm disks are also flattened, but vertically thicker than thin disks. Another clear difference between them is that warm disks are likely to be centrally concentrated, while some cold disks have an obvious central break (e.g., Sb_10, Sa_10, and Sa_11). Both bulges and halos are slowly rotating spheroids. Our models thus confirm that dynamically cold stars in galaxies with high j_z/j_c always form a flattened, diskly structure, and that dynamically hot stars with low j_z/j_c form a spheroidal structure. Kinematic halos extend into the galaxy center. This implies that bulges decomposed from their morphology should be the superposition of intrinsic bulges and halos.

To better quantify the morphology, we measure the one-dimensional stellar surface density profiles for each structure obtained using classification 1. The top panels of Figures 6 and 7 show the face-on and edge-on views of the galaxy, respectively. As expected, both cold (blue) and warm disks (green) have somewhat exponential profiles. Bulges (red) are compact, and halos (magenta) extend farther out to large radius following a nearly Sérsic function. However, the morphologies of diskly structures, especially warm disks, are still quite complex using this classification. Cold disks are largely truncated in their central regions, while many warm disks seem to host an additional component that is much more compact than their outer regions (e.g., Sa_10.5, Sb_10.5, Sc_10.5, Sa_11, and Sb_11). An extra compact component associated with the warm disk can also clearly be seen in the two-dimensional face-on images of these models (Figure 5). Thus, there is no simple way that the morphologies of the kinematic structures can be described with this classification method.

4.2. Classification 2: Including a Diskly Bulge

The central concentrations, common in many warm disks and in some cold disks, strongly suggest that our classification method 1 has failed to isolate an important, additional

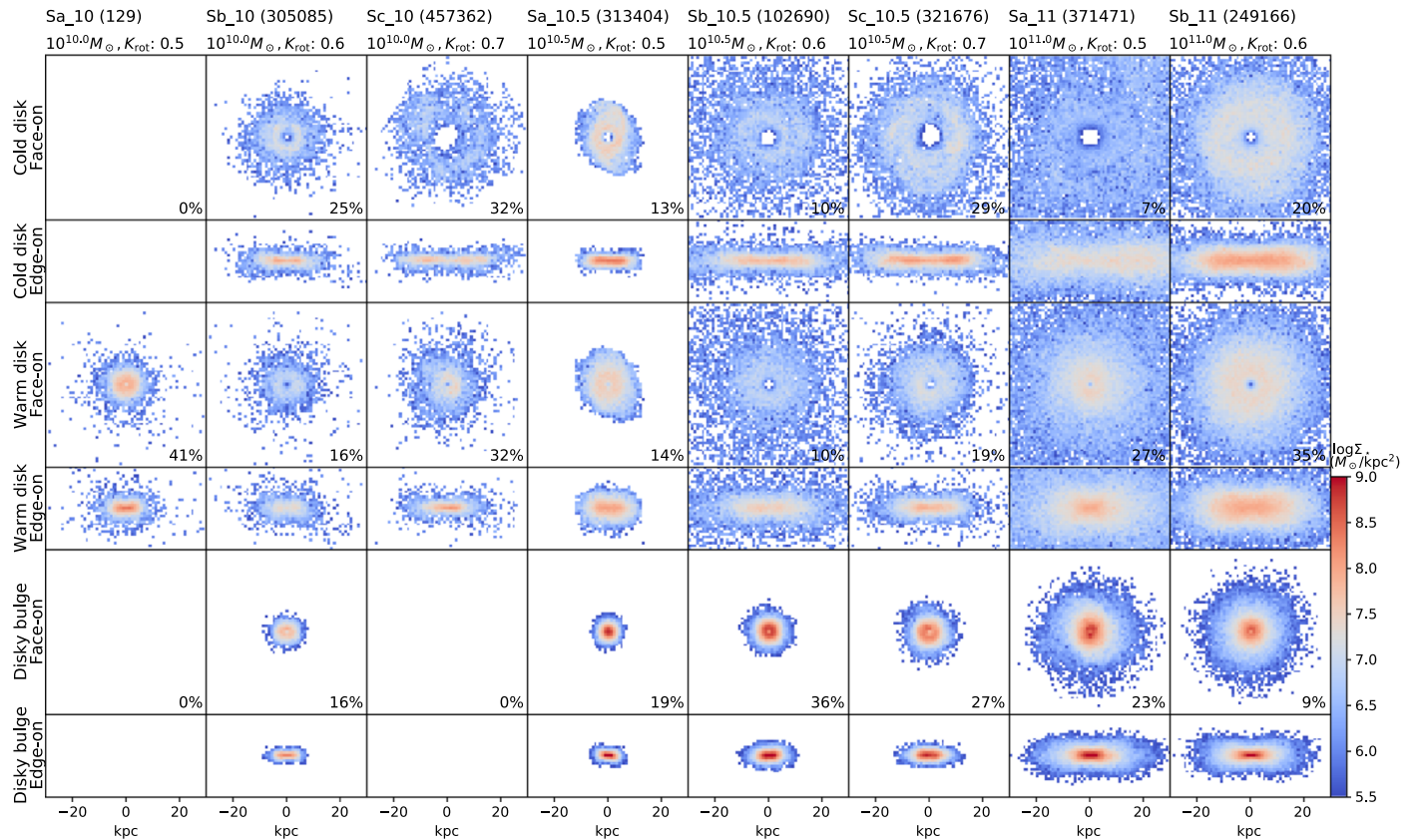


Figure 8. Kinematic structures of examples selected from TNG100, classified according to method 2; the galaxies are the same as those shown in Figure 5. From top to bottom, we show the face-on and edge-on views of the surface density distributions of the cold disk, warm disk, and diskly bulge. The mass ratios of each structure, labeled in the bottom-right corner of each panel, are estimated from stars within $3r_e$.

component. This additional component—characterized by moderate rotation and a centrally concentrated morphology—motivates us to add another structure that is likely located at the bottom-right corner of the $\langle j_z/j_c \rangle$ versus $\langle e/|e|_{\max} \rangle$ diagram (marked by the dotted square in Figures 3 and 4). We name this new structure the “disky bulge,” and we designate this method of `auto-GMM` classification as classification 2. We show the one-dimensional surface density profiles of the structures identified by classification 2 in the bottom panels of Figures 6 and 7 for comparison with those identified by classification 1. The bulge and halo structures are exactly the same in the two methods, while the extra central concentrations of cold and warm disks in classification 1 are assigned as diskly bulges under classification 2. Removing the central concentration simplifies the density distributions of both the cold and warm disks. The diskly bulge component accounts for roughly half of the mass of the warm disk. The two-dimensional stellar surface density distributions of these diskly structures are shown in Figure 8. The flatten morphology and moderate rotation of diskly bulges (bottom panels of Figure 8; see Section 5.2.2 for the statistic results) strongly suggest that they are the counterparts of the so-called pseudo-bulges frequently observed (e.g., Kormendy & Kennicutt 2004).

It is worth emphasizing that the differences between warm disks and diskly bulges are not always significant. In Figure 3, there is no clear gap between the groups of the diskly bulge and the warm disk. Although the separation of the diskly bulge from disks helps to gain more freedom for comparing with

morphological decompositions, it is unclear whether they form through a different mechanism. This topic lies beyond the scope of this paper.

4.3. Fitting the Kinematic Structures of Classification 2

As shown in the bottom panels of Figures 6 and 7, all kinematic structures derived from classification 2 seem to follow regular morphologies that can be well-described as a Sérsic or truncated exponential function. The exponential function can be truncated by a hyperbolic function (Peng et al. 2010):

$$T = 0.5 \left(\tanh \left[(2 - B) \frac{R}{R_b} + B \right] + 1 \right), \quad (1)$$

where $B = 2.65 - 4.98 R_b / (R_b - R_s)$, with R_b the break radius and R_s the softening in the cylindrical coordinate system. Only stars within 3 half-mass radii are used. The minimum density of each bin is limited to $10^6 M_\odot \text{ kpc}^{-2}$ (about one stellar particle per 1 kpc^2). We also ignore the region $R \leq 1 \text{ kpc}$ in the fitting, in order to avoid the oversmoothing effect in the central region whose size is similar to the softening length (0.7 kpc) of the stars.

The fit results (solid profiles) of the selected examples are overlaid in the bottom panels of Figures 6 and 7. The best-fitting function is selected automatically based on χ^2 ,

defined as

$$\chi^2 = \frac{1}{N} \sum_{i=0}^N \left(\frac{\Sigma_{*,i} - \Sigma_{\text{model},i}}{\Sigma_{*,i}} \right)^2, \quad (2)$$

where $\Sigma_{*,i}$ and $\Sigma_{\text{model},i}$ are the average surface density of the data and model, respectively. It is clear that all structures can be well-fitted, suggesting that the kinematic structures, when converted into radial mass surface density profiles, can be robustly captured by the functional forms traditionally used for photometric morphological components.

5. Statistical Properties of Kinematic Structures

Kinematic parameters that quantify the relative importance of circular rotation have been widely used to decompose spheroidal components from disks in simulated galaxies (e.g., Sales et al. 2010; Tacchella et al. 2019). However, the relation between morphological and kinematic measurements is still fairly unclear, possibly leading to contradictory conclusions. For example, Huertas-Company et al. (2019) found that the morphologies of both high-mass and low-mass galaxies in TNG100 are in tension with visual morphologies of observed nearby galaxies. In particular, they found an overabundance of late-type galaxies ($\sim 50\%$ versus $\sim 20\%$) at the high-mass end ($M_* > 10^{11} M_\odot$). In contrast, Tacchella et al. (2019) concluded that both the mass fraction and concentration of spheroidal components identified by kinematics agree fairly well with observations.

In this section, we study the statistical properties of intrinsic kinematic structures identified by `auto-GMM`. To link kinematic and morphological structures, we also decompose the disk galaxies morphologically, adopting a simple model comprising an exponential function for the disk and a Sérsic function for the bulge, as is commonly applied to observed galaxy images. We use the mass-based one-dimensional face-on surface density profiles. Thus, the effects of dust and the change of mass-to-light ratio are not considered, the same as the kinematic decomposition. In observations, the effects of dust on galaxy morphology is generally minimized via selecting dust-free galaxy samples or using redder bandpasses (e.g., Salo et al. 2015; Gao et al. 2020). Again, we ignore the central region ($R \leq 1$ kpc) due to the low resolution. This model works adequately for most of our galaxies.

5.1. Mass Fraction

Based on the hierarchical framework illustrated in Figure 1, we can easily estimate the properties of the kinematic structures. The mass fraction of the spheroid of each galaxy is given in the top panel of Figure 9 by summing up the masses of the bulge and halo. The red, blue, and black solid profiles represent, respectively, the medians of elliptical,⁸ disk, and all galaxies of $M_* \geq 10^{10} M_\odot$. The shaded regions indicate their 1σ scatter. The mass fraction of spheroids (black solid profile) clearly rises from 0.5 to 0.9 with increasing galaxy mass. This change is consistent with the sharp drop in the number of disk galaxies at $M_* \approx 10^{10.6} M_\odot$, as shown in the bottom panel. Both the trend and scatter of spheroid mass fraction are perfectly consistent with the results of Tacchella et al. (2019; dashed line with error bars), who also adopted a kinematic

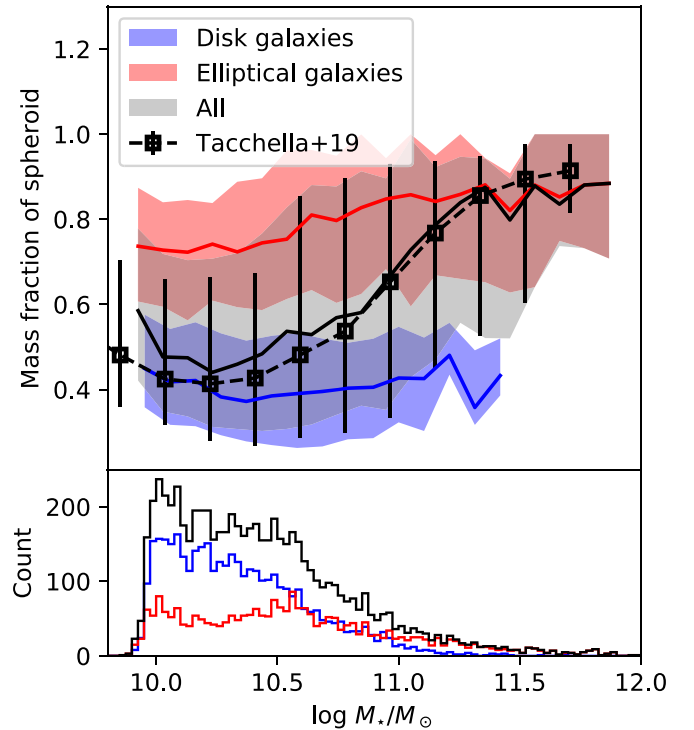


Figure 9. Mass fractions of spheroidal structures in TNG100 galaxies. All galaxies of stellar mass $\geq 10^{10} M_\odot$ are included. The parent sample is classified into disk and elliptical galaxies with the criterion $K_{\text{rot}} = 0.5$. The solid profiles represent the median, while the shaded regions are the envelopes of 1σ scatter. The spheroids include the bulges and halos identified kinematically by `auto-GMM`. Here, M_* and mass fraction are measured from stars within $3r_e$, to facilitate comparison with previous results and observations. The mass fractions of spheroids obtained by `auto-GMM` are consistent with the results of Tacchella et al. (2019). The number count of galaxies in each mass bin is shown in the bottom panel.

approach. This trend is also consistent with the photometric bulge+disk decomposition of 7500 local galaxies in the GAMA survey (Moffett et al. 2016), as suggested by Tacchella et al. (2019). Similarly, Park et al. (2019) showed that kinematically derived spheroids contribute to 43% of total stellar mass in 144 field galaxies at $z = 0.7$ in the New Horizon simulation (a zoom-in simulation of Horizon-AGN; Y. Dubois et al. 2020, in preparation). Taking our sample of disk galaxies as a whole, spheroids contribute $\sim 40\%$ – 50% (the blue profile in the top panel of Figure 9), roughly independent of stellar mass for the mass range considered here.

Figure 10 explores the mass fractions of the various kinematic structures in greater detail. The difference between barred and unbarred galaxies can be seen by comparing the dashed and dotted profiles. It is clear that the mass fraction of bulges is lower in less massive galaxies ($M_* \lesssim 10^{10.7} M_\odot$). The stellar halo mass fraction becomes more prominent in massive galaxies, possibly due to the increase of diffuse spheroids produced in dry mergers, as the amount of accreted stellar mass increases significantly in galaxies above $\sim 10^{10.5} M_\odot$ (Rodríguez-Gomez et al. 2016; Pillepich et al. 2018a). Our two classification schemes produce exactly the same bulges and halos, their main differences manifesting only in terms of the cold and warm disks.

The disk structures identified through our kinematic method contribute a constant mass fraction in the disk galaxies. Using classification 1, the cold disk comprises 20%, with a scatter of $\pm 10\%$. The average mass fraction of warm disks is higher than

⁸ We have also applied `auto-GMM` to decompose elliptical galaxies, even though they are generally featureless.

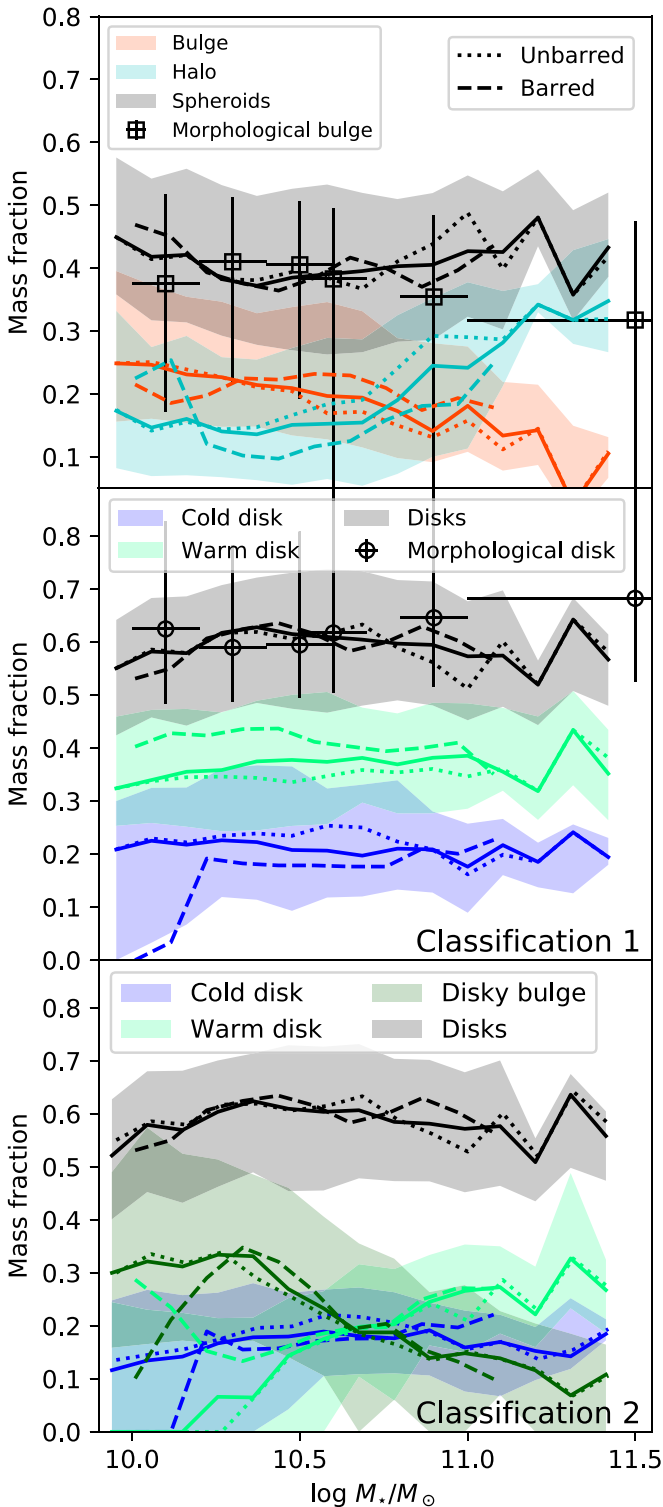


Figure 10. Mass fractions of kinematic structures identified by `auto-GMM` in TNG100 disk galaxies. The solid profiles represent the median, while the shaded regions are the envelopes of 1σ scatter. Both M_* and mass fraction are measured from stars within $3r_e$. The results of disk structures obtained using classifications 1 and 2 are shown in the middle and bottom panels, respectively. The dotted and dashed profiles represent the medians of unbarred and barred galaxies, respectively. Barred galaxies are likely to host more bulges and warm disks, and thus less massive halos and cold disks. The squares and circles with error bars mark the mass fractions of bulges and disks, respectively, obtained from a simple bulge+disk decomposition of the mass distribution.

that of cold disks by 75%. The mass fractions of both cold and warm disks are almost independent of galaxy stellar mass. The cold and warm disk mass fractions we obtain are similar to those extracted in CALIFA galaxies using the Schwarzschild method, for which Zhu et al. (2018b) estimate $\sim 20\%$ and 40% , respectively. However, it is worth mentioning that Zhu et al. (2018b) measured luminosity fractions within $1r_e$. Over the same scales, `auto-GMM` obtains cold disk fractions $\lesssim 10\%$, pointing to possible systematic discrepancies between these two methods. Alternatively, stars are overheated in the central regions in the TNG100 galaxies, due to its low resolution. We intend to investigate this issue in the future using higher resolution runs of `IllustrisTNG` (i.e., TNG50).

Classification 2 yields a roughly constant cold disk mass fraction of 15%, somewhat lower than that estimated by classification 1. The warm disk mass fraction rises with total galaxy mass, from nearly 0% to about 30%.

The trends for bulges and halos are the same using classification 2. The frequency of both cold and warm disks decreases significantly in low-mass galaxies, as a consequence of the separation of disky bulges from cold and warm disks, leading to the significant decrease of warm disk mass fraction and the large scatter of cold disk mass fraction toward low-mass galaxies (bottom panel of Figure 10).

The mass fractions of bulges and disks derived from traditional morphological decomposition (squares and circles in Figure 10) are consistent with the mass fractions decomposed kinematically. However, the kinematically decomposed spheroids also include halos, whose morphologies are likely to be different from bulges. The kinematic bulges alone comprise only half or less of the mass fraction of morphological bulges. Morphologically identified bulges cannot be linked directly to either kinematic spheroids or bulges. Thus, while the observed bulge+disk morphology is generally indeed an indicator of the underlying stellar kinematics, it is still unlikely to be an accurate proxy of the diverse kinematic structures that are mixed in galaxies. In order to link the morphological and kinematic structures, their density profiles are compared in detail in the next section.

Compared to their unbarred counterparts, barred galaxies have $\sim 5\%$ – 10% higher mass fractions in warm disks and bulges. This is partially due to the misclassification of stars moving on bar orbits (Du et al. 2019), although genuine differences between the two galaxy types cannot be excluded. For the purposes of this study, we simply note that the differences between barred and unbarred galaxies are smaller than their 1σ scatter and do not affect any of our main results.

5.2. Radial Surface Density Profiles

To better understand the relation between the kinematic structures found by `auto-GMM` and morphological structures, we compare the radial density distributions of the kinematic structures with the bulges and disks derived from traditional morphological decomposition.

5.2.1. Morphological Decomposition: Bulge+Disk

Figure 11 shows the one-dimensional surface density profiles as a function of radius. The panels, from left to right, give the

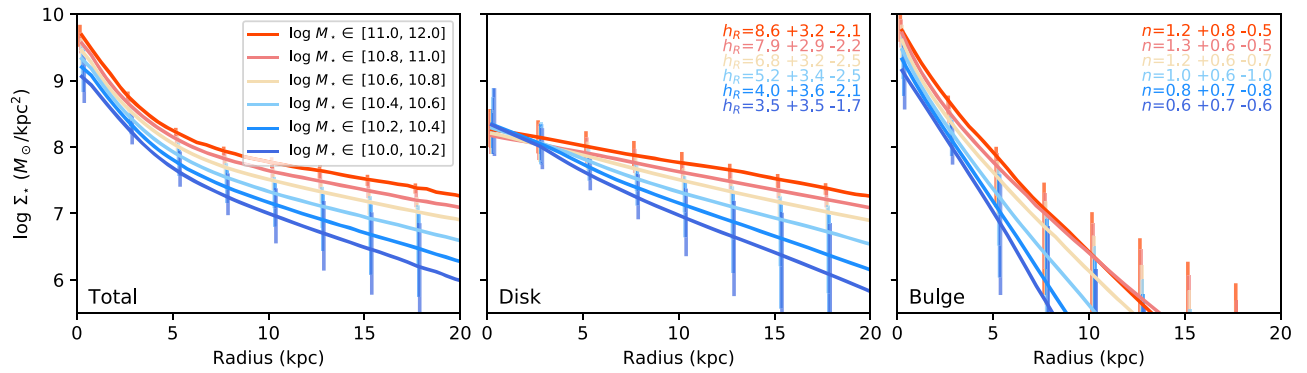


Figure 11. Radial surface density profiles of $z = 0$ disk galaxies from TNG100. We separate the galaxies into equal mass bins of 0.2 dex, except for the most massive ones. From left to right, the panels show the median surface density profiles of the entire galaxy, the exponential disk component alone, and the Sérsic bulge component alone, decomposed using the morphological method. The error bars represent the 1σ scatter. To avoid overlap, we shift the error bars slightly for clarity.

face-on surface density profiles of the entire galaxy, the exponential disk alone, and the Sérsic bulge alone.

The disks have reasonable scale lengths that increase with galaxy mass, from $h_R = 3.5^{+3.5}_{-1.7}$ to $7.9^{+2.9}_{-2.2}$ kpc. This trend is roughly consistent with observations of galaxies over the stellar mass range 10^{10} – $10^{11} M_\odot$ (e.g., Fathi et al. 2010). The Sérsic index of the bulge component increases from $n = 0.9^{+0.7}_{-0.4}$ in lower mass, $M_* = 10^{10} M_\odot$ galaxies to $n = 1.4^{+0.6}_{-0.4}$ in galaxies of $M_* = 10^{11} M_\odot$. A Sérsic index of $n < 2$ is generally used to separate pseudo-bulges from classical ones (e.g., Fisher & Drory 2008, but see Gao et al. 2020). Very few bulges with $n > 2$ exist in TNG100 disk galaxies. Fitting the overall surface luminosity with a single Sérsic function, Rodriguez-Gomez et al. (2019) showed that TNG100 generates lower values of n with respect to Pan-STARRS observations of nearby galaxies. Our results reaffirm this trend and extend it explicitly to the scale of the bulge. On the other hand, the simulated galaxies have spheroidal components that are roughly consistent with observations (Figure 9), suggesting that TNG100 generates similar but systematically less compact spheroids. It is unclear to what extent these results are affected by our ignoring the central 1 kpc region (because of resolution effects), and a fuller investigation must await analysis of higher resolution simulations.

5.2.2. Kinematic Decomposition

Figures 12 and 13 examine the face-on surface density profiles for the kinematic structures, dividing the galaxies into six bins of total stellar mass. The median profiles from the morphological bulge+disk decomposition are overlaid for comparison. In Figure 12, the density profiles of disks (upper-left panel) are obtained by summing all kinematically disky structures (the cold and warm disks identified using classification 1), while those of spheroids (bottom-left panel) include both the halos and bulges. Both cold disks and warm disks (top panels) follow nearly exponential profiles with classification 1. However, cold disks are truncated in their inner regions, while warm disks are overmassive in their inner parts. This is consistent with the morphologies of the examples shown in Section 4.1. Some cold disks have similarly central overmassive components as well. As discussed in Section 4.2, this is a clear imprint of the presence of disky bulges.

As suggested in Section 4.2, it is necessary to separate disky bulges from other disky structures in order to explain the extra central concentrations. The location of disky bulges in the

distribution of kinematic moments is marked by the dotted square in Figure 3. Once we consider the disky bulge as a new, separate structure, the surface density profiles of cold and warm disks become simpler (Figure 13). The warm disk follows a similar exponential profile as the cold disk, but it is clearly more centrally concentrated, with a smaller central truncation.⁹ There are no central overmassive components present for cold and warm disks in galaxies of different stellar masses. The combined surface densities of cold and warm disks (upper-left panel of Figure 12) also follow exponential profiles. From a kinematic point of view, disky bulges are essentially disky structures. They rotate like warm disks. However, from the perspective of morphology, disky bulges are more similar to bulges (upper-right panel of Figure 13). Both of these traits are reminiscent of pseudo-bulges (e.g., Kormendy & Kennicutt 2004).

The density profiles of bulges and halos are exactly the same in classifications 1 and 2, shown in the bottom panels of Figure 12. The spheroidal structures of bulge+halo does not match morphological bulges well. In order to reconstruct morphological bulges, we show all possible combinations of the kinematic structures obtained by classification 2 in the bottom panels of Figure 13. It is clear that morphological bulges match best the inner region ($R \lesssim 5$ kpc) of the case of the bulge+halo+disky bulge. This suggests that morphological bulges are composite structures of bulges, halos, and disky bulges decomposed by kinematics. The relative contribution of these three components to morphological bulges is shown in Figure 14. Clearly, kinematic bulges dominate in the very central regions. The importance of disky bulges and halos increases outward. In face-on views (top panels), at $R \approx 2$ kpc, the disky bulges have a comparable importance with kinematic bulges, then start to dominate toward larger radius. The kinematic halos contribute about one-third of the mass of morphological bulges at $R \leq 3$ kpc and increases slowly outward. The same ratios but viewed edge on are given in the bottom panels of Figure 14. The disky bulges, which are flattened structures, become more prominent due to the projection. The contribution of kinematic bulges reduces to ~ 0.45 at $R = 1$ kpc.

Our result is somewhat consistent with the well-known idea that bulges have two subtypes (classical and pseudo). But classical bulges seem to coexist with both disky pseudo-bulges and halos. Thus, the intrinsic kinematic structures may be

⁹ Zhu et al. (2018c) also reported similar central truncations of disk orbits in the galaxies of the CALIFA survey.

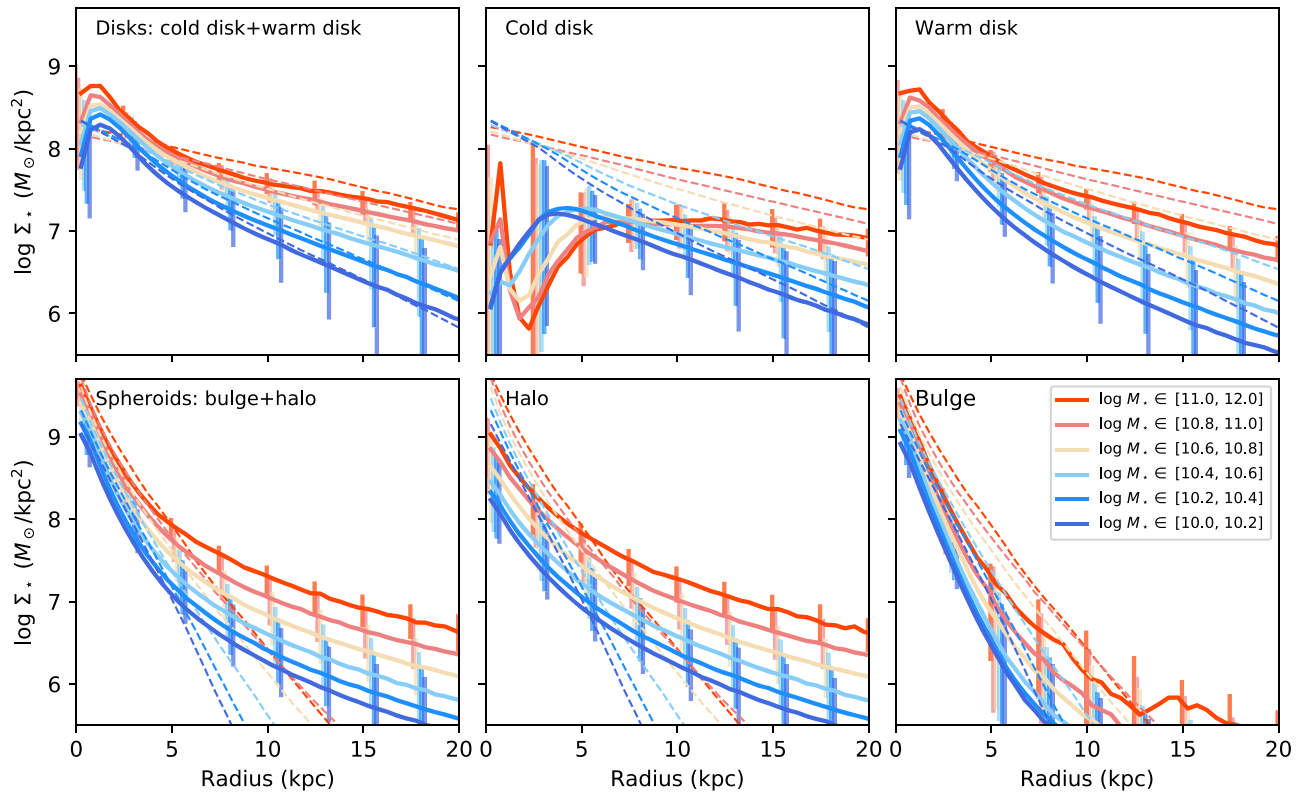


Figure 12. Radial surface density profiles of kinematic structures decomposed by `auto-GMM` in $z = 0$ disk galaxies from TNG100. Four structures are identified by classification 1. The spheroids are obtained by summing up bulges and halos, while the combination of cold and warm disks are the disks. The sample of disk galaxies is the same as that shown in Figure 11, separated into the equal mass bins. The error bars (slightly shifted for clarity) represent the 1σ scatter. The dashed median profiles of the morphological disks (top panels) and bulges (bottom panels) are overlaid to compare with the results of the kinematic decomposition.

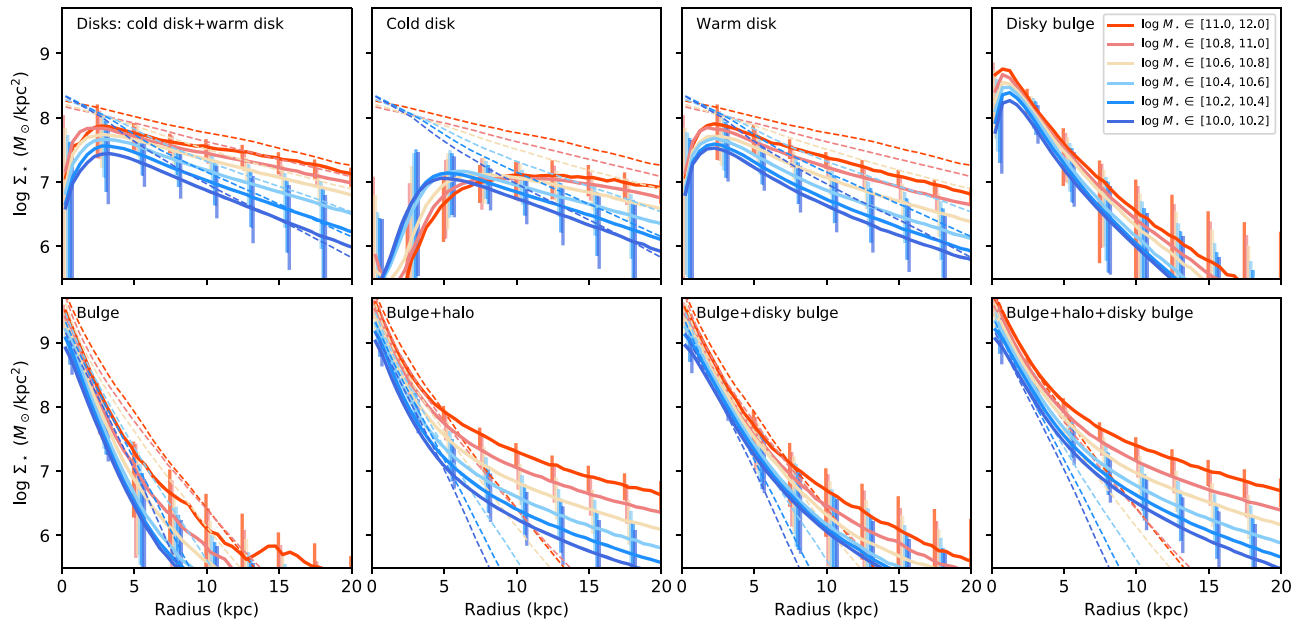


Figure 13. Radial surface density profiles of kinematic structures identified by `auto-GMM` in $z = 0$ disk galaxies from TNG100. We use the same sample as in Figure 12, but adopt classification 2, and hence disky bulges are separated from disks. The solid profiles represent the median, and the error bars are the 1σ scatter. For comparison, we overlay the density profiles of the morphological disks (top panels) and bulges (bottom panels). In the bottom panels, we compare, from left to right, the surface density distribution between the morphological bulge with the kinematic bulge, the composite of bulge+halo, bulge+disky bulge, and bulge+halo+disky bulge. Clearly, the inner part of composite structure of bulge+halo+disky bulge best matches the morphological bulge.

significantly mixed from a morphological point of view. Recently, some composite bulge systems have been found via detailed morphological decompositions of nearby galaxies (Nowak et al. 2010; Méndez-Abreu et al. 2014; Erwin et al.

2015). Generally, compact, dynamically hot inner classical bulges were found to be embedded in pseudo-bulges. The Sérsic indices of such classical bulges are generally small ($n < 2$; Erwin et al. 2015). These are qualitatively consistent

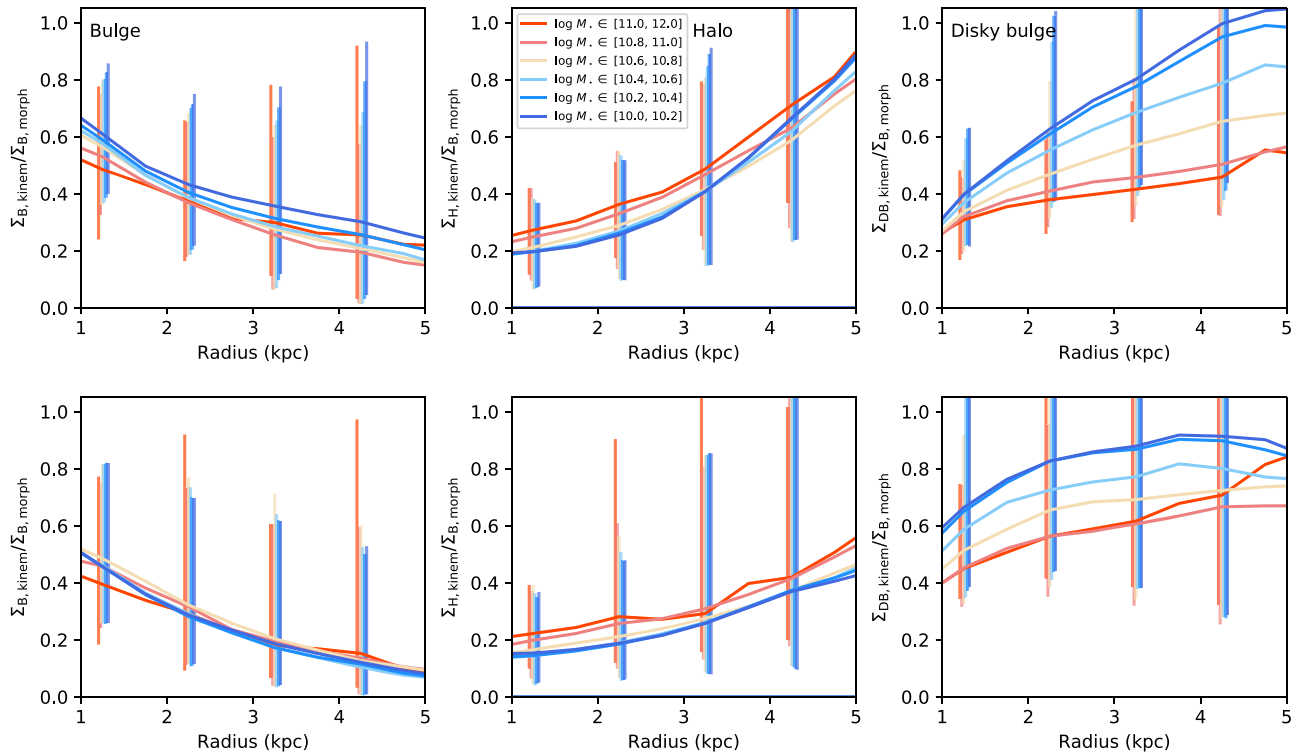


Figure 14. Fractional radial deviation of morphological structures from kinematic structures identified by `auto-GMM` via classification 2 for different mass bins, for bulges (B), halos (H), and disk bulges (DB), from left to right. The denominators are the surface densities of morphological bulges (B, morph). The top and bottom panels are measured in the face-on and edge-on views, respectively. The solid profiles represent the median, and the error bars are their 1σ scatter. The values within 1 kpc are ignored.

with the composite bulges we obtain in `IllustrisTNG` galaxies.

6. Conclusions

Du et al. (2019) presented an automated method, `auto-GMM`, that can decompose galactic structures efficiently for simulated galaxies based on their kinematic phase-space properties. A few examples covering a broad range in mass and morphology show that `auto-GMM` recovers reasonable structures in an unsupervised way. Here, we apply this method to a large sample of present-day galaxies from the cosmological simulation `IllustrisTNG`. A sample of about 4000 disk galaxies of stellar mass $10^{10-11.6} M_{\odot}$, one-fourth of which are barred, is selected from TNG100 to analyze the statistical properties of structures identified by `auto-GMM` and to provide general insights into the relationship between kinematically and morphologically derived galactic structures. Such structures fall into a clear pattern in the kinematic phase space of normalized azimuthal angular momentum (circularity), nonazimuthal angular momentum, and binding energy. Thus, they are likely to be intrinsic structures.

Two methods are introduced to classify the kinematic structures. The so-called “classification 2” gives five kinds of intrinsic kinematic structures: cold disks, warm disks, disk bulges, bulges, and halos whose kinematic and morphological properties are qualitatively consistent with thin disks, thick disks, pseudo-bulges, classical bulges, and halos defined by morphology, i.e., profile fitting, in observations. We define cold and warm disks as disk structures having strong and moderate rotation, respectively. The stars of both bulges and halos distribute in spheroidal morphologies, but those of bulges are clearly more tightly bound. In “classification 1,” disk bulges are considered as

part of disks that generally have a similar rotation to warm disks; however, their compact morphologies motivate us to separate them from disk structures in classification 2.

Across all TNG100 $z = 0$ disk galaxies of $10^{10-11.6} M_{\odot}$, the kinematic spheroidal structures, obtained by summing up stars of bulges and halos, contribute about $\sim 40\%$ – 50% of the total stellar mass within $3r_c$; the disk structures (cold disks, warm disks, and disk bulges) make up the remainder. The mass fraction of kinematic spheroids is consistent with the mass fraction of bulges decomposed via the morphological method. However, a systematic comparison between morphological and kinematic structures shows that they have significant differences in their morphologies.

The bulges decomposed by morphology exhibit a composite structure that includes $\sim 60\%$ kinematic bulges, $\sim 20\%$ halos, and $\sim 30\%$ disk bulges at $R \approx 1$ kpc in face-on view. At $R \approx 2$ kpc, disk bulges become equally important ($\sim 40\%$ of total stellar mass) to kinematic bulges in morphological bulges. Moreover, disk bulges are essentially disk structures that have a similar rotation to warm disks and are likely to be classified as pseudo-bulges in observations. Furthermore, our results indicate that classical bulges commonly coexist with disk pseudo-bulges.

The mixtures of multiple structures are less substantial in disks. Warm disks are generally more centrally concentrated than cold disks. The most surprising result is that most cold disks and many warm disks are sharply truncated in the galaxy central regions. The truncation radius of cold disks generally happens around 5 kpc in lower mass galaxies, while it happens at larger radii in massive ones. A similar phenomenon can be seen in a high-resolution galaxy simulation of the Milky Way

(Buck et al. 2019, Figure 2). This suggests that the disk mass of the inner regions of galaxies is possibly significantly over-estimated by a simple exponential fitting that is widely used in observations. Similarly, Zhu et al. (2018c) concluded that the central region of spiral galaxies is dominated by warm components rather than cold or hot components. Furthermore, we find that kinematic halos contribute $\sim 30\%$ of the mass of the outer part of morphological disks in face-on view.

Galaxy structures identified via morphological methods (e.g., profile fitting of the photometry) may not reflect intrinsic galaxy components because of the underlying complexity of the stellar populations, the reduced information content of the images, e.g., with respect to kinematics constraints, and the risks of human bias. Cosmological simulations of galaxies are a powerful tool to identify galaxies' intrinsic structures and subcomponents and to relate them to physical processes. However, in order to be a reliable source of insights, the simulations need to return galaxies whose structures and properties are as realistic as possible. Despite the remarkable success achieved by TNG100, it remains challenging to make qualitative and quantitative comparisons with observations in detail, largely due to the resolution limitation. In future work, we will extend this analysis to high redshifts and the highest resolution run of the IllustrisTNG series (TNG50 Nelson et al. 2019b; Pillepich et al. 2019). The formation and evolution of each structure found in this work will be studied in greater detail.

This work was supported by the National Science Foundation of China (11721303, 11991052) and the National Key R&D Program of China (2016YFA0400702). M.D. is also supported by the National Postdoctoral Program for Innovative Talents (8201400810) and the Postdoctoral Science Foundation of China (8201400927) from the China Postdoctoral Science Foundation. V.P.D. was supported by STFC Consolidated grant ST/R000786/1. V.P.D. acknowledges support from the Kavli Visiting Scholars Program for a visit to the KIAA during this work. D.Y.Z. acknowledges the support by the Peking University Boya Fellowship. The TNG100 simulation used in this work, one of the flagship runs of the IllustrisTNG project, was run on the HazelHen Cray XC40-system at the High Performance Computing Center Stuttgart as part of project GCS-ILLU of the Gauss Centres for Supercomputing (GCS). The authors thanks all the members of the IllustrisTNG team for making the IllustrisTNG data available to us prior to their public release. We also thank Ling Zhu and Dandan Xu for constructive discussions. This work made use of the High-performance Computing Platform of Peking University. The analysis was performed using Pynbody (Pontzen et al. 2013).

ORCID iDs

Min Du  <https://orcid.org/0000-0001-9953-0359>
 Luis C. Ho  <https://orcid.org/0000-0001-6947-5846>
 Victor P. Debattista  <https://orcid.org/0000-0001-7902-0116>
 Annalisa Pillepich  <https://orcid.org/0000-0003-1065-9274>
 Dongyao Zhao  <https://orcid.org/0000-0001-8592-7910>
 Lars Hernquist  <https://orcid.org/0000-0001-6950-1629>

References

Abadi, M. G., Navarro, J. F., Steinmetz, M., & Eke, V. R. 2003, *ApJ*, 597, 21
 Agertz, O., Teyssier, R., & Moore, B. 2011, *MNRAS*, 410, 1391
 Algorry, D. G., Navarro, J. F., Abadi, M. G., et al. 2017, *MNRAS*, 469, 1054

Andredakis, Y. C., Peletier, R. F., & Balcells, M. 1995, *MNRAS*, 275, 874
 Andredakis, Y. C., & Sanders, R. H. 1994, *MNRAS*, 267, 283
 Aumer, M., White, S. D. M., Naab, T., & Scannapieco, C. 2013, *MNRAS*, 434, 3142
 Bland-Hawthorn, J., & Gerhard, O. 2016, *ARA&A*, 54, 529
 Brook, C. B., Stinson, G. S., Gibson, B. K., et al. 2012, *MNRAS*, 426, 690
 Buck, T., Ness, M., Obreja, A., Macciò, A. V., & Dutton, A. A. 2019, *ApJ*, 874, 67
 Cappellari, M., Emsellem, E., Krajnović, D., et al. 2011a, *MNRAS*, 413, 813
 Cappellari, M., Emsellem, E., Krajnović, D., et al. 2011b, *MNRAS*, 416, 1680
 Colín, P., Avila-Reese, V., Roca-Fàbrega, S., & Valenzuela, O. 2016, *ApJ*, 829, 98
 Comerón, S., Elmegreen, B. G., Salo, H., et al. 2014, *A&A*, 571, A58
 Comerón, S., Knapen, J. H., Sheth, K., et al. 2011, *ApJ*, 729, 18
 Courteau, S., de Jong, R. S., & Broeils, A. H. 1996, *ApJL*, 457, L73
 Crain, R. A., Schaye, J., Bower, R. G., et al. 2015, *MNRAS*, 450, 1937
 Dalcanton, J. J., & Bernstein, R. A. 2002, *AJ*, 124, 1328
 Davis, M., Efstathiou, G., Frenk, C. S., & White, S. D. M. 1985, *ApJ*, 292, 371
 Diaz-García, S., Salo, H., Laurikainen, E., & Herrera-Endoqui, M. 2016, *A&A*, 587, A160
 Doménech-Moral, M., Martínez-Serrano, F. J., Domínguez-Tenreiro, R., & Serna, A. 2012, *MNRAS*, 421, 2510
 Du, M., Ho, L. C., Zhao, D., et al. 2019, *ApJ*, 884, 129
 Dubois, Y., Peirani, S., Pichon, C., et al. 2016, *MNRAS*, 463, 3948
 Elmegreen, B. G., Elmegreen, D. M., Tompkins, B., & Jenks, L. G. 2017, *ApJ*, 847, 14
 Emsellem, E., Cappellari, M., Krajnović, D., et al. 2007, *MNRAS*, 379, 401
 Emsellem, E., Cappellari, M., Krajnović, D., et al. 2011, *MNRAS*, 414, 888
 Erwin, P. 2018, *MNRAS*, 474, 5372
 Erwin, P., Saglia, R. P., Fabricius, M., et al. 2015, *MNRAS*, 446, 4039
 Eskridge, P. B., Frogel, J. A., Pogge, R. W., et al. 2000, *AJ*, 119, 536
 Fathi, K., Allen, M., Boch, T., Hatziminaoglou, E., & Peletier, R. F. 2010, *MNRAS*, 406, 1595
 Fisher, D. B., & Drory, N. 2008, *AJ*, 136, 773
 Gao, H., Ho, L. C., Barth, A. J., & Li, Z.-Y. 2020, *ApJS*, 247, 20
 Gargiulo, I. D., Monachesi, A., Gómez, F. A., et al. 2019, *MNRAS*, 489, 5742
 Genel, S., Nelson, D., Pillepich, A., et al. 2018, *MNRAS*, 474, 3976
 Genel, S., Vogelsberger, M., Springel, V., et al. 2014, *MNRAS*, 445, 175
 Grand, R. J. J., Gómez, F. A., Marinacci, F., et al. 2017, *MNRAS*, 467, 179
 Guedes, J., Callegari, S., Madau, P., & Mayer, L. 2011, *ApJ*, 742, 76
 Hopkins, P. F., Kereš, D., Oñorbe, J., et al. 2014, *MNRAS*, 445, 581
 Hopkins, P. F., Wetzell, A., Kereš, D., et al. 2018, *MNRAS*, 480, 800
 Huertas-Company, M., Rodríguez-Gomez, V., Nelson, D., et al. 2019, *MNRAS*, 489, 1859
 Kass, R., & Raftery, A. 1995, *J. Am. Statist. Ass.*, 90, 773
 Knapen, J. H., Shlosman, I., & Peletier, R. F. 2000, *ApJ*, 529, 93
 Kormendy, J., & Kennicutt, R. C., Jr. 2004, *ARA&A*, 42, 603
 Krajnović, D., Alatalo, K., Blitz, L., et al. 2013, *MNRAS*, 432, 1768
 Ma, X., Hopkins, P. F., Wetzell, A., et al. 2017, *MNRAS*, 467, 2430
 Marinacci, F., Pakmor, R., & Springel, V. 2014, *MNRAS*, 437, 1750
 Marinacci, F., Vogelsberger, M., Pakmor, R., et al. 2018, *MNRAS*, 480, 5113
 Marinova, I., & Jogee, S. 2007, *ApJ*, 659, 1176
 Méndez-Abreu, J., Debattista, V. P., Corsini, E. M., & Aguerri, J. A. L. 2014, *A&A*, 572, A25
 Méndez-Abreu, J., Simonneau, E., Aguerri, J. A. L., & Corsini, E. M. 2010, *A&A*, 521, A71
 Menéndez-Delmestre, K., Sheth, K., Schinnerer, E., Jarrett, T. H., & Scoville, N. Z. 2007, *ApJ*, 657, 790
 Moffett, A. J., Lange, R., Driver, S. P., et al. 2016, *MNRAS*, 462, 4336
 Murante, G., Monaco, P., Borgani, S., et al. 2015, *MNRAS*, 447, 178
 Naiman, J. P., Pillepich, A., Springel, V., et al. 2018, *MNRAS*, 477, 1206
 Nelson, D., Kauffmann, G., Pillepich, A., et al. 2018, *MNRAS*, 477, 450
 Nelson, D., Pillepich, A., Genel, S., et al. 2015, *A&C*, 13, 12
 Nelson, D., Pillepich, A., Springel, V., et al. 2019a, *MNRAS*, 490, 3234
 Nelson, D., Pillepich, A., Springel, V., et al. 2019b, *MNRAS*, 490, 3234
 Nelson, D., Springel, V., Pillepich, A., et al. 2019c, *ComAC*, 6, 2
 Nowak, N., Thomas, J., Erwin, P., et al. 2010, *MNRAS*, 403, 646
 Obreja, A., Dutton, A. A., Macciò, A. V., et al. 2019, *MNRAS*, 487, 4424
 Obreja, A., Macciò, A. V., Moster, B., et al. 2018, *MNRAS*, 477, 4915
 Obreja, A., Stinson, G. S., Dutton, A. A., et al. 2016, *MNRAS*, 459, 467
 Pakmor, R., Bauer, A., & Springel, V. 2011, *MNRAS*, 418, 1392
 Pakmor, R., Springel, V., Bauer, A., et al. 2016, *MNRAS*, 455, 1134
 Park, M.-J., Yi, S. K., Dubois, Y., et al. 2019, *ApJ*, 883, 25
 Pedregosa, F., Varoquaux, G., Gramfort, A., et al. 2011, *Journal of Machine Learning Research*, 12, 2825, <http://jmlr.org/papers/v12/pedregosa1a.html>

- Peng, C. Y., Ho, L. C., Impey, C. D., & Rix, H.-W. 2010, *AJ*, **139**, 2097
- Pillepich, A., Nelson, D., Hernquist, L., et al. 2018a, *MNRAS*, **475**, 648
- Pillepich, A., Nelson, D., Springel, V., et al. 2019, *MNRAS*, **490**, 3196
- Pillepich, A., Springel, V., Nelson, D., et al. 2018b, *MNRAS*, **473**, 4077
- Pontzen, A., Roškar, R., Stinson, G. S., et al. 2013, pynbody: Astrophysics Simulation Analysis for Python, Astrophysics Source Code Library, ascl:1305.002
- Pop, A.-R., Pillepich, A., Amorisco, N., & Hernquist, L. 2017, *Galax*, **5**, 34
- Pop, A.-R., Pillepich, A., Amorisco, N. C., & Hernquist, L. 2018, *MNRAS*, **480**, 1715
- Rodríguez-Gomez, V., Pillepich, A., Sales, L. V., et al. 2016, *MNRAS*, **458**, 2371
- Rodríguez-Gomez, V., Snyder, G. F., Lotz, J. M., et al. 2019, *MNRAS*, **483**, 4140
- Rosas-Guevara, Y., Bonoli, S., Dotti, M., et al. 2020, *MNRAS*, **491**, 2547
- Roškar, R., Teyssier, R., Agertz, O., Wetzstein, M., & Moore, B. 2014, *MNRAS*, **444**, 2837
- Sales, L. V., Navarro, J. F., Schaye, J., et al. 2010, *MNRAS*, **409**, 1541
- Salo, H., Laurikainen, E., Laine, J., et al. 2015, *ApJS*, **219**, 4
- Sánchez, S. F., Kennicutt, R. C., Gil de Paz, A., et al. 2012, *A&A*, **538**, A8
- Sandage, A., Tammann, G. A., & McFarland, J. 1981, *IrAJ*, **15**, 61
- Schaye, J., Crain, R. A., Bower, R. G., et al. 2015, *MNRAS*, **446**, 521
- Schulze, F., Remus, R.-S., Dolag, K., et al. 2018, *MNRAS*, **480**, 4636
- Schwarzschild, M. 1979, *ApJ*, **232**, 236
- Springel, V. 2010, *MNRAS*, **401**, 791
- Springel, V., Pakmor, R., Pillepich, A., et al. 2018, *MNRAS*, **475**, 676
- Springel, V., White, S. D. M., Tormen, G., & Kauffmann, G. 2001, *MNRAS*, **328**, 726
- Stinson, G. S., Bovy, J., Rix, H.-W., et al. 2013, *MNRAS*, **436**, 625
- Tacchella, S., Diemer, B., Hernquist, L., et al. 2019, *MNRAS*, **487**, 5416
- Toomre, A. 1977, in *Evolution of Galaxies and Stellar Populations*, ed. B. M. Tinsley, R. B. G. Larson, & D. Campbell (New Haven, CT: Yale Univ. Observatory), 401
- Valluri, M., Merritt, D., & Emsellem, E. 2004, *ApJ*, **602**, 66
- van den Bosch, R. C. E., van de Ven, G., Verolme, E. K., Cappellari, M., & de Zeeuw, P. T. 2008, *MNRAS*, **385**, 647
- Vogelsberger, M., Genel, S., Springel, V., et al. 2014a, *MNRAS*, **444**, 1518
- Vogelsberger, M., Genel, S., Springel, V., et al. 2014b, *Natur*, **509**, 177
- Vogelsberger, M., Marinacci, F., Torrey, P., & Puchwein, E. 2020, *NatRP*, **2**, 42
- Wang, L., Dutton, A. A., Stinson, G. S., et al. 2015, *MNRAS*, **454**, 83
- Weinberger, R., Springel, V., Hernquist, L., et al. 2017, *MNRAS*, **465**, 3291
- Xu, D., Zhu, L., Grand, R., et al. 2019, *MNRAS*, **489**, 842
- Yoachim, P., & Dalcanton, J. J. 2006, *AJ*, **131**, 226
- Yun, K., Pillepich, A., Zinger, E., et al. 2019, *MNRAS*, **483**, 1042
- Zhou, Z.-B., Zhu, W., Wang, Y., & Feng, L.-L. 2020, arXiv:2004.11620
- Zhu, L., van de Ven, G., Leaman, R., et al. 2019, arXiv:2003.05561
- Zhu, L., van de Ven, G., Méndez-Abreu, J., & Obreja, A. 2018a, *MNRAS*, **479**, 945
- Zhu, L., van de Ven, G., van den Bosch, R., et al. 2018b, *NatAs*, **2**, 233
- Zhu, L., van den Bosch, R., van de Ven, G., et al. 2018c, *MNRAS*, **473**, 3000
- Zhu, Q., Xu, D., Gaspari, M., et al. 2018d, *MNRAS*, **480**, L18